

1 **theRma1UAV: an R package to clean and correct thermal UAV data for accurate land**
2 **surface temperatures**

3 Christophe Metsu^{a,*}, Wouter H. Maes^b, Sam Ottoy^{a,c,d}, Koenraad Van Meerbeek^{a,e}

4 ^a *Division Forest, Nature and Landscape, Department Earth and Environmental Sciences, KU Leuven, 3000 Leuven, Belgium*

5 ^b *UAV Research Centre, Department of Plants and Crops, Ghent University, 9000 Ghent, Belgium*

6 ^c *Bio-Research, PXL University College, 3590 Diepenbeek, Belgium*

7 ^d *Center for Environmental Sciences, Hasselt University, 3590 Diepenbeek, Belgium*

8 ^e *KU Leuven Plant Institute, KU Leuven, 3000 Leuven, Belgium*

9 ^{*} *Corresponding author. christophe.metsu@kuleuven.be*

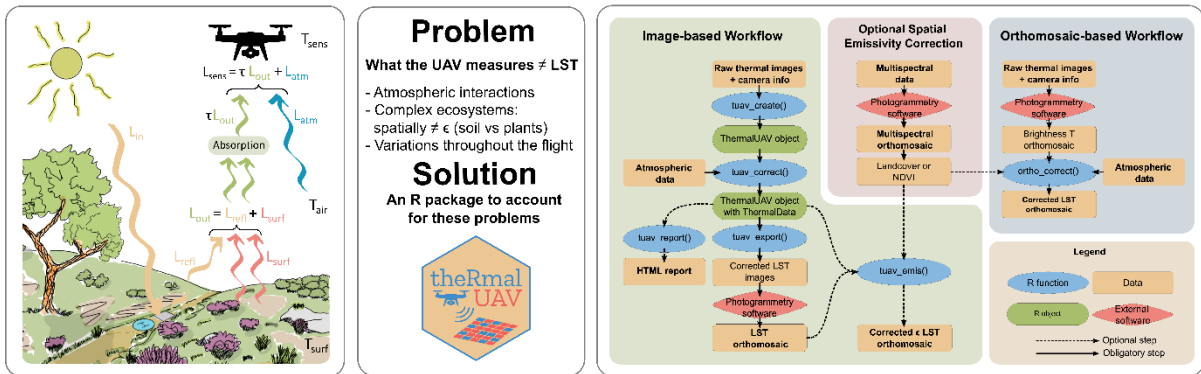
10 **Keywords:** Drones, Remote Sensing, Thermal Infrared, TIR, UAS, Unmanned Aerial Systems,
11 Unoccupied Aerial Vehicles

12 **Abstract**

13 Thermal cameras mounted on unoccupied aerial vehicles (UAVs) are increasingly utilized across various
14 environmental research fields, including hydrological modelling, wildfire detection, urban heat island
15 studies, microclimate and precision agriculture. However, several steps are needed to convert the
16 measured thermal signal to more relevant land surface temperature (LST). Since a number of users
17 may have limited expertise in thermal remote sensing or data processing, necessary thermal
18 corrections are often neglected or not performed correctly in research, even though this can result in
19 substantial discrepancies of up to 5 °C in extreme cases when absolute LST is required. We facilitate
20 the processing by introducing a new R package, `theRma1UAV`, which offers two workflows: an
21 orthomosaic-based and an image-based workflow. The orthomosaic workflow consists of a single
22 function to apply on an orthomosaic, while the image-based workflow provides greater flexibility,
23 accommodating intra-flight variations in atmospheric conditions. Key components of the package
24 include correcting for atmospheric interactions, background temperature, spatial emissivity using
25 NDVI and land cover, and the influence of changing weather conditions on LST. Additionally, we
26 introduce a novel method for accounting for rapid changes in illumination during flights. The package
27 also includes functions for data cleaning, co-registration, and reporting. The package currently
28 supports 11 different thermal sensors, covering the vast majority of thermographic cameras used
29 today. The importance of these corrections and the implementation of the package are demonstrated
30 through two use cases involving TeAx and DJI thermal cameras, under both ideal and challenging
31 conditions.

theRmalUAV: an R package to clean and correct thermal UAV data

Christophe Metsu, Wouter H. Maes, Sam Ottoy, Koenraad Van Meerbeek



32

33 1. Introduction

34 Surface temperature is a critical variable across various domains, ranging from industrial applications
35 to environmental studies. It serves as a key parameter in describing the energy balance between a
36 surface and its surroundings, primarily due to its direct relationship with emitted long-wave infrared
37 radiation (LWIR, 8-14 μm). This energy balance, or derived thermal metrics, can provide deeper
38 insights into the properties and processes occurring within the corresponding object. Surface
39 temperature has a broad spectrum of applications. In search and rescue missions, it is utilized to locate
40 missing persons or track wildlife (Rudol and Doherty, 2008). In industrial contexts, it is employed for
41 inspecting solar panels (Liao and Lu, 2021; Vlamincx et al., 2022), monitoring power lines (Dai et al.,
42 2025), and identifying thermal leaks in buildings (Rakha et al., 2018).

43 Moreover, surface temperature is invaluable in environmental research and applications. Its potential
44 is being explored in diverse fields, including hydrological modelling (Aicardi et al., 2017), coastal water
45 quality estimation (Cheng et al., 2022), evaporation estimation (Hoffmann et al., 2016), urban heat
46 island studies (Henn and Peduzzi, 2024; Wu et al., 2022), wildfire detection (Allison et al., 2016), and
47 land use modelling (Muro et al., 2018). It is also used for wildlife population estimation (Beaver et al.,
48 2020; Mirka et al., 2022), identification of microclimatic refugia (Hoffrén and García, 2023), and
49 vegetation monitoring. In precision agriculture, surface temperature is directly applied in the crop
50 water stress index to detect stress and diseases (Messina and Modica, 2020; Santesteban et al., 2017;
51 Stutsel et al., 2021).

52 Advancements in remote sensing technologies have led to cost reductions and the miniaturization of
53 sensors, thereby promoting the increased utilization of unoccupied aerial vehicles (UAVs or drones) in
54 environmental research (Manfreda et al., 2018). Compared to traditional handheld thermal cameras
55 or thermal satellite imagery, UAVs provide high spatial resolution and flexibility, enabling the
56 acquisition of spatially continuous datasets with very high resolution. The integration of thermal
57 infrared cameras on UAV platforms allows for the measurement of incoming LWIR and the direct

58 derivation of land surface temperatures (LST).

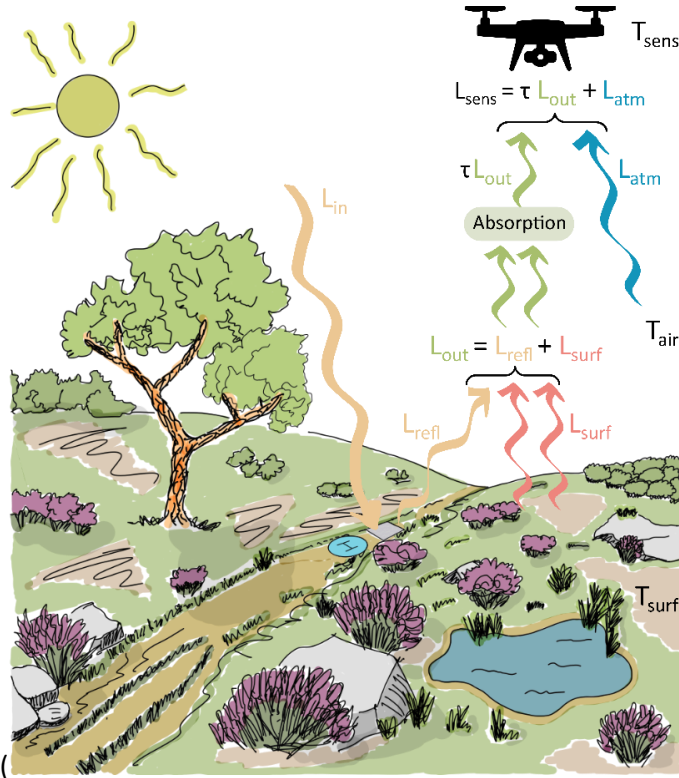
59 In instances where precise absolute temperatures are required, the temperature data obtained from
60 UAVs (or other remote sensing platforms) may not provide an immediately accurate product. The
61 reliability of the data is significantly affected by variability in camera accuracy, surface properties, and
62 atmospheric conditions, leading to a discrepancy between LST and the temperature measured at the
63 sensor. Consequently, thermal infrared data acquired from UAVs often require essential corrections.

64 The complexity of the necessary corrections and the potential lack of thorough background in thermal
65 remote sensing among environmental scientists and other UAV researchers, often result in incomplete
66 or incorrect application of these corrections. Therefore, we have developed the user-friendly R
67 package `theRmalUAV` for cleaning and correcting thermal UAV data. The aim of this package is to
68 facilitate the implementation of fundamental corrections necessary to obtain optimal results from UAV
69 thermal imagery. The methods and workflow are partially based on the recommendations of Maes,
70 Huete and Steppe (2017), and Heinemann et al. (2020), with additional new functionalities. To help
71 users understand the features offered in this package, we will first provide an overview of some basic
72 principles of thermal remote sensing and the key concepts employed in the package. Subsequently,
73 we will discuss the general workflow and capabilities of the package and showcase its application in
74 two use cases with different sensors (Section 4 and 5).

75 **2. Thermal remote sensing background**

76 Typical thermal infrared (TIR, 8-14 μm) cameras used on UAV platforms are based on microbolometer
77 sensor arrays. This type of sensor is a thermistor radiation detector, which relates the absorbed
78 incoming TIR radiation energy to the temperature-dependent electrical resistance of the material.
79 They do not require expensive cooling, in contrast to alternative high-resolution photonic IR sensors,
80 making them more cost-effective (Posch et al., 2009; Wood et al., 1992). Uncooled TIR cameras,
81 however, require extensive and complex calibration processes, which are usually already implemented
82 by the manufacturer, adding to the cost of the camera (Budzier and Gerlach, 2015). Such calibration
83 establishes a relationship between the electrical resistance of a pixel of the uncooled microbolometer
84 sensor, expressed as grey values, and the corresponding blackbody temperature. The temperature
85 data are then stored as digital numbers (DN), usually as integers in a 16 or 32-bit tiff file format. To
86 convert these DN values into usable temperatures in Kelvin or degrees Celsius, a linear constant is
87 applied. The resulting temperature is referred to as the at-sensor temperature.

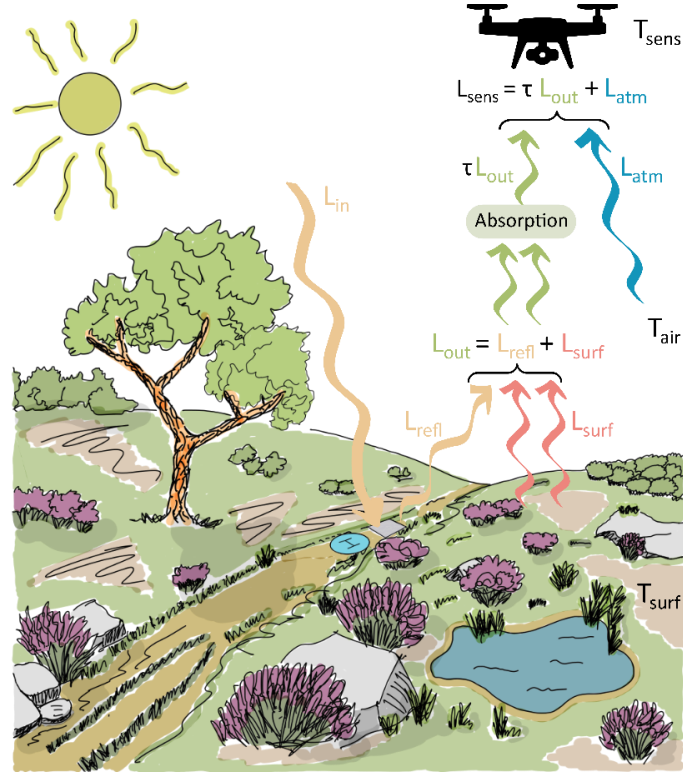
88 For most applications, the at-sensor temperature is not yet the desired temperature. The incoming TIR
 89 radiation at the sensor includes multiple components, which can be described with the following



90 radiative transfer model (Figure 1; Jones and Vaughan, 2010):
 91

$$L_{sens} = \tau (L_{surf} + L_{refl}) + L_{atm} \quad (1)$$

92 L_x represents the radiance, i.e. the amount of radiation energy emitted, reflected, transmitted, or
 93 received by a given surface, per unit solid angle, per unit projected area, per unit time ($W\ m^{-2}\ sr^{-1}$), of
 94 the corresponding TIR radiation of property "x". In the radiative transfer model, L_{sens} stands for the
 95 radiance reaching the sensor, L_{surf} the radiance from the TIR radiation emitted by the surface, L_{refl}
 96 describes the fraction of downwelling TIR radiation reflected by the surface ($1 - \epsilon$) and L_{atm} represents
 97 the upwelling TIR radiation emitted by the atmospheric layer between the surface and the camera.
 98 The radiation passing through the atmospheric layer is attenuated, which is accounted for by the
 99 atmospheric transmittance τ (value between 0 and 1). Furthermore, L_{sens} depends on both the
 100 wavelength and sensor-specific properties (e.g. the wavelength range to which the sensor is sensitive).
 101 Therefore, the TIR camera manufacturer considers a modified inverse Planck function when converting
 102 L_{sens} to the at-sensor temperature (T_{sens}), typically assuming transmittance and emissivity to be one
 103 (Heinemann et al., 2020).



104

105 *Figure 1. Visual representation of the TIR radiation components received by thermal sensor. L_{sens} denotes the radiance*
 106 *reaching the sensor ($W m^{-2} sr^{-1}$) and consists of (i) L_{atm} , representing the upwelling TIR radiation emitted by the atmospheric*
 107 *layer between the surface and the sensor, influenced by the free air temperature (T_{air}), (ii) L_{surf} , the radiance from the TIR*
 108 *radiation emitted by the surface, influenced by the surface temperature (T_{surf}), and (iii) L_{refl} , given by the fraction of*
 109 *downwelling/incoming TIR radiation (L_{in}) reflected by the surface. L_{refl} and L_{surf} are represented together as L_{out} and are both*
 110 *partially absorbed by the atmosphere, taken into account by the atmospheric transmittance τ . T_{sens} stands for the temperature*
 111 *perceived by the sensor (i.e., at-sensor temperature).*

112 Natural objects are not perfect blackbodies, an idealized physical object that absorbs and emits all
 113 incident radiation. The degree to which an object absorbs and emits TIR radiation compared to a
 114 perfect black body at the same temperature is described by its emissivity (ϵ), ranging from 0 to 1.
 115 Consequently, the proportion of TIR radiation that is reflected is its complement:

$$L_{refl} = (1 - \epsilon) L_{in} \quad (2)$$

116 The relationship between radiant energy emitted by natural surfaces and their absolute temperature
 117 is described by the Stefan-Boltzmann law (Jones and Vaughan, 2010):

$$L_{surf} = \epsilon \sigma T_{surf}^4 \quad (3)$$

118 where L_{surf} represents the amount of radiation energy emitted by the surface, per unit projected area,
 119 per unit time ($W m^{-2}$), ϵ is the emissivity, σ is the Stefan-Boltzmann constant ($5.67 \cdot 10^{-8} W m^{-2} K^{-4}$), and
 120 T_{surf} is the absolute temperature of the surface in Kelvin. Based on Eqs (1), **Error! Reference source not**
 121 **found.** and as outlined in Maes, Huete and Steppe (2017) and Heinemann et al. (2020), the retrieval
 122 of LST can be formulated as follows:

$$LST = T_{surf} = \sqrt[4]{\frac{T_{sens}^4 - (1-\epsilon) \tau T_{bg}^4 - \frac{L_{atm}}{\sigma}}{\epsilon \tau}} \quad (4)$$

123 where T_{surf} is the desired LST of a surface with emissivity ϵ , T_{sens} the at-sensor temperature measured
 124 by the TIR camera, and T_{bg} the background temperature (to account for L_{refl} , see Section 2.2), all
 125 expressed in Kelvin. The emissivity (ϵ) and transmittance (τ) range between 0 and 1, and L_{atm} represents
 126 the upwelling TIR radiation emitted by the atmospheric layer between the surface and the sensor. L_{atm}
 127 can be described using the following equation:

$$L_{atm} = (1 - \tau) \sigma T_{air}^4 \quad (5)$$

128 with τ as the transmittance, and σ the Stefan-Boltzmann constant. T_{air} is the temperature of the
 129 atmospheric layer between the surface and the sensor (in Kelvin). As this is hard to quantify for the
 130 whole layer, the assumption is made that T_{air} is equal to the temperature at 1.5 - 2 meters height, and
 131 can therefore be measured by a weather station. According to Eq. (5), Eq. (4) becomes:

$$LST = T_{surf} = \sqrt[4]{\frac{T_{sens}^4 - (1-\epsilon) \tau T_{bg}^4 - (1-\tau) T_{air}^4}{\epsilon \tau}} \quad (6)$$

132 Following Eq. (6), the calculation of LST requires, next to the at-sensor temperature and surface specific
 133 emissivity, also some atmospheric properties, like transmittance, background temperature, and free
 134 air temperature. In the next sections we will go over the atmospheric correction, the concept of
 135 background temperature and emissivity correction.

136 2.1. Atmospheric correction

137 The atmospheric conditions during a thermal UAV flight exert a substantial influence on the TIR
 138 radiation received by the sensor, e.g. due to water vapor absorption, and thus the measured at-sensor
 139 temperature. Flying during humid, overcast conditions compared to a dry, sky clear day may result in
 140 different outputs for the same T_{surf} . After performing atmospheric correction to account for these
 141 conditions, the resulting temperature data is commonly referred to as brightness temperature:

$$T_{brightness} = \sqrt[4]{\frac{T_{sens}^4 - (1-\tau) T_{air}^4}{\tau}} \quad (7)$$

142 The transmittance of the atmosphere quantifies the proportion of L_{out} that can actually reach the
 143 thermal camera (Figure 1). It can be calculated using Eqs. (8),(9), by implementing parameters, like free
 144 air temperature (T_{air} (K), i.e. the temperature of the atmospheric layer between the surface and the
 145 sensor) and relative humidity ($\omega\%$, i.e. the amount of water vapor in the air compared to the maximum
 146 amount the air can hold at a given temperature), which can be retrieved from in situ measurements
 147 or nearby weather stations. First, the water vapor content (ω , in mm) is calculated based on relative
 148 humidity and air temperature:

$$\omega = \omega\% \exp(h_1 T_{air}^3 + h_2 T_{air}^2 + h_3 T_{air} + h_4) \quad (8)$$

149 where $\omega\%$ is the relative humidity ranging from 0 to 1, and T_{air} is the free air temperature ($^{\circ}\text{C}$). In
 150 addition, h_1 , h_2 , h_3 , and h_4 are specific parameters defined for the temperature window from -40 to

151 120 °C, where $h_1 = 6.8455 \times 10^{-7}$, $h_2 = -2.7816 \times 10^{-4}$, $h_3 = 6.939 \times 10^{-2}$, and $h_4 = 1.5587$ (Minkina and
 152 Klecha, 2015; Tran et al., 2017). Subsequently, transmittance (τ) can be computed using the water
 153 vapor content and the distance between the sensor and the measured object (d , in m):

$$\tau = K_{atm} \exp[-\sqrt{d}(\alpha_1 + \beta_1\sqrt{\omega})] + (1 - K_{atm}) \exp[-\sqrt{d}(\alpha_2 + \beta_2\sqrt{\omega})] \quad (9)$$

154 with K_{atm} a specific scaling factor of atmospheric damping, representing the combined effect of
 155 absorption by gaseous components and the atmospheric turbidity ($K_{atm} = 1.9$), together with the
 156 atmospheric attenuation without water vapor ($\alpha_1 = 0.0066$, $\alpha_2 = 0.0126$), and the attenuation of water
 157 vapor ($\beta_1 = -0.0023$, $\beta_2 = -0.0067$) (Minkina and Klecha, 2015; Tran et al., 2017). The distance between
 158 the sensor and the measured object is a measure of the amount of atmosphere which interferes with
 159 the radiation.

160 2.2. Background temperature and emissivity correction

161 To account for the atmospheric conditions above the UAV, and therefore the reflected downwelling
 162 TIR radiation (L_{refl} , Figure 1), the concept of background temperature (T_{bg}) can be used, representing
 163 the “temperature of the sky”. This can be easily determined by retrieving the corresponding brightness
 164 temperature of a panel covered with (crumpled) aluminium foil using the TIR camera (Maes, Huete
 165 and Steppe, 2017; Heinemann et al., 2020). Due to its emissivity of typically less than 0.03, aluminium
 166 foil reflects almost all TIR radiation (Frolec et al., 2019). The sensor thus measures all TIR radiation
 167 emitted by the sky.

168 When T_{bg} is not measured, it can be estimated using the air temperature (Maes and Steppe, 2012):

$$T_{bg} = \sqrt[4]{\epsilon_{clr} F T_{air}^4} \quad (10)$$

169 with T_{bg} the background temperature, ϵ_{clr} the sky emissivity at clear sky, T_{air} the air temperature in
 170 Kelvin, and F a measure of the cloudiness of the sky (where $F \geq 1$). A commonly used value for ϵ_{clr} is
 171 0.7 (Sedlar and Hock, 2009). Under clear sky conditions, F equals 1, thus a T_{air} value of 20 °C (293.15
 172 K) corresponds to a T_{bg} of -5 °C (268.15 K). In overcast conditions, F approximates 1.4, bringing T_{bg} in
 173 line with T_{air} .

174 Following from Eq. (3), (4), emissivity is a crucial parameter for relating surface temperature to the
 175 measured LWIR, describing the extent to which the surface deviates from a black body. Emissivity has
 176 the largest impact of all parameters in Eq. (6) on obtaining accurate LST (Maes and Steppe, 2012); an
 177 error of 1% in emissivity corresponds to a temperature difference of 0.75K (Jones et al., 2003) in sunny
 178 conditions. This influence becomes even more significant in sunny conditions and with lower emissivity
 179 values (see the example in Section 4). However, obtaining the correct emissivity value is very
 180 challenging and usually two major assumptions are being made. First, emissivity is assumed to be
 181 constant in the spectral range of 8-14 μm , although it is wavelength-dependent, varying slightly across

182 this range (Salisbury and D’Aria, 1992). Second, angular effects are ignored to simplify the retrieval
 183 methods, even though emissivity varies with the viewing angle (Cuenca and Sobrino, 2004). Emissivity
 184 is often estimated using indirect methods, such as lookup tables, empirical relationships with other
 185 metrics, or by solving radiometric equations (Li and Becker, 1993; Van de Griend and Owe, 1993). It
 186 should be noted that the emissivity of individual objects, such as leaves, can be measured. However,
 187 the emissivity of vegetation as a whole differs from that of individual vegetation components and is
 188 generally higher due to the shadow cavities within the vegetation, which resemble black boxes. Thus,
 189 emissivity at the vegetation level cannot be directly measured (Maes and Steppe, 2012).

190 While using one fixed value might be ok for a homogenous surface, this approach is too simplistic in
 191 more complex ecosystems. The implementation of vegetation indices, such as the NDVI (the
 192 normalized difference vegetation index), enable spatially explicit estimation of thermal emissivity by
 193 applying an empirical relationship between the index and thermal emissivity (Kerr et al., 2004). The
 194 NDVI is given by:

$$NDVI = \frac{NIR-R}{NIR+R} \quad (11)$$

195 with NIR and R the reflectance of near-infrared and red radiation respectively and lies between -1 to
 196 1. It can be useful to differentiate between vegetation densities, as well as land cover types by setting
 197 simple thresholds. Valor and Caselles (1996) proposed a method where emissivity is given as a function
 198 of vegetation and bare soil emissivity values with vegetation cover fraction as weight:

$$\epsilon = \epsilon_{veg} P_v + \epsilon_{soil} (1 - P_v) + d\epsilon \quad (12)$$

199 where P_v is the vegetation cover fraction, ϵ_{veg} is the vegetation emissivity, ϵ_{soil} the bare soil emissivity,
 200 and $d\epsilon$ a term due to cavity effect (surface roughness). This term can be written as $d\epsilon =$
 201 $4 \langle d\epsilon \rangle P_v (1 - P_v)$, where $\langle d\epsilon \rangle$ is a simplified parameter ($\langle d\epsilon \rangle \approx 0.01$). The vegetation cover fraction
 202 can simply be determined by (Carlson and Ripley, 1997; Sobrino et al., 2008):

$$P_v = \left(\frac{NDVI - NDVI_{soil}}{NDVI_{veg} - NDVI_{soil}} \right)^2 \quad (13)$$

203 with $NDVI_{veg}$ and $NDVI_{soil}$ the NDVI of respectively full vegetation and bare soil. This way of prediction
 204 the emissivity is used in the NDVI threshold method (Sobrino and Raissouni, 2000). By setting two well-
 205 chosen NDVI thresholds, the landscape can be divided into three classes: bare soil, vegetation, and
 206 mixed pixels, where the latter relies on Eq. (12) to estimate the emissivity. The NDVI threshold method
 207 is often used because of its simplicity and already successfully applied to various sensors (Li et al.,
 208 2013), such as AVHRR (Sobrino and Raissouni, 2000) and MODIS (Sobrino et al., 2003). Moreover, the
 209 need for accurate atmospheric corrections when calculating P_v is not necessary because of the use of
 210 a normalized vegetation index (Li et al., 2013). A downside is the assumption that the surface only
 211 consists of soil and vegetation (e.g., water is not taken into the equation) (Tang et al., 2015).

212 Furthermore, a priori knowledge on ϵ_{veg} , ϵ_{soil} , $NDVI_{veg}$, and $NDVI_{soil}$ is needed. The method is not limited
213 to soil and vegetation and can for example be used to create an emissivity gradient between healthy,
214 green and dead or senescent vegetation using emissivity values as described in Salisbury and D’Aria
215 (1992).

216 The classification-based emissivity method is another approach to account for the spatial variation in
217 emissivity. In essence, a land cover classification is performed and the corresponding emissivity values
218 are assigned to each class (Li et al., 2013). This method heavily relies on the accuracy of the
219 classification and possible limitations in number of classes. Furthermore, relevant emissivity values are
220 available in databases like Salisbury and D’Aria (1992). In general, dense vegetation has a high
221 emissivity value between 0.98 and 0.99 (Rubio et al., 1997). However, it is also related to the state of
222 the vegetation and can, for example, substantially decrease for dry vegetation (Lillesand et al., 2015).

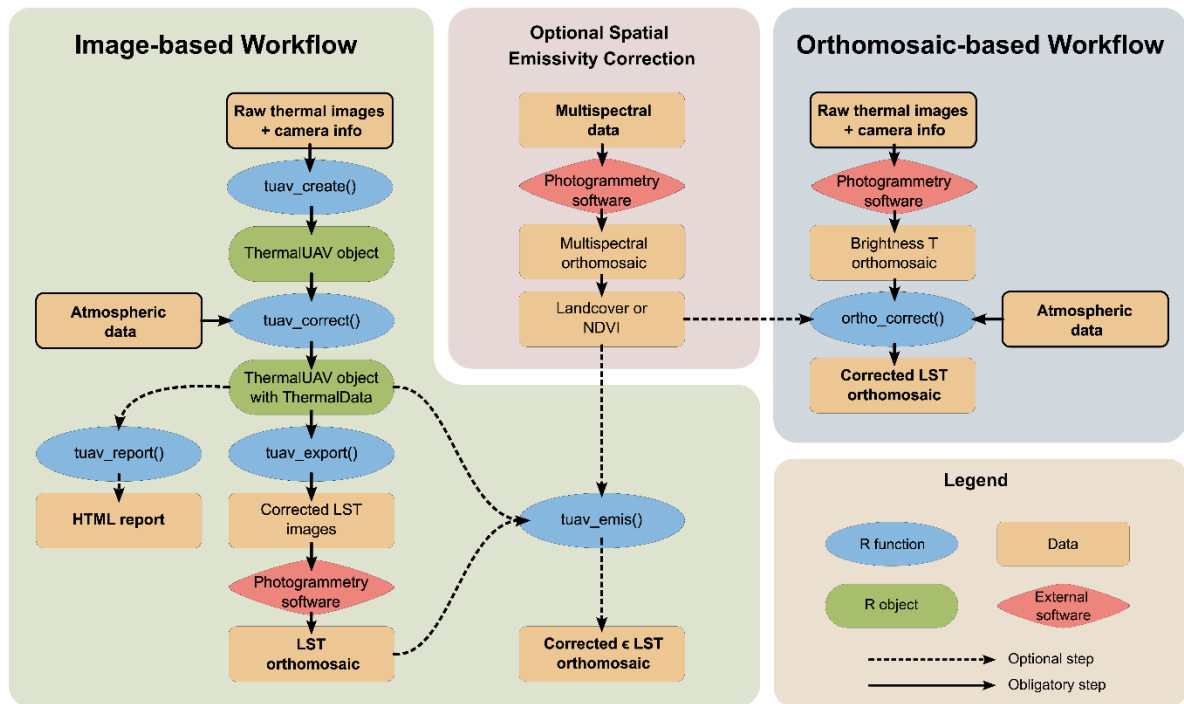
223 **3. The `therma1UAV` workflow and functionalities**

224 The R package can be installed from [[christophemetsu/theRmalUAV: An R package to clean and correct](https://github.com/christophemetsu/theRmalUAV)
225 [thermal UAV data](#)]. The functionalities of the `theRmalUAV` package are grouped into two workflows
226 (Figure 2):

- 227 1. **Image-based workflow:** streamlines individually correcting thermal images before combining
228 them into an orthomosaic using external photogrammetry software. This approach allows for
229 adjustments to temperature and relative humidity variations over prolonged flight durations.
- 230 2. **Orthomosaic-based workflow:** performs the corrections directly on an already stitched
231 brightness temperature orthomosaic. The workflow is intended for scenarios where processing
232 of the individual raw thermal images is either unnecessary or unfeasible (e.g., due to a lack of
233 weather station data). In this context, intra-flight atmospheric variability is not considered.
234 However, this workflow is particularly beneficial for multispectral cameras where the thermal
235 band has a low resolution and relies on other bands for stitching in photogrammetry software
236 (e.g. Micasense Altum).

237 In both workflows, users have the option to include a spatially explicit emissivity correction if
238 multispectral data or a land cover map is available, though this is optional, it is highly recommended.
239 In the image-based workflow, the `tuav_emis()` post-processing function is used to correct a LST
240 orthomosaic created following the image-based workflow. In the orthomosaic-based workflow, on the
241 other hand, the spatially explicit emissivity correction is directly embedded in the `ortho_correct()`
242 function.

243 Figure 2 provides an overview of the core functions of both workflows and their most important steps
 244 are discussed below. More advanced functionalities and options are discussed in Section 3.2.5, 3.2.6
 245 and 3.4. Additional information is available in the vignettes of the R package and on the website.



246
 247 *Figure 2. Overview of the theRmalUAV workflows. The green box presents the image-based workflow where raw thermal*
 248 *images are converted in corrected LST images. The othomosaic-based workflow is presented in the blue box, converting a*
 249 *brightness temperature orthomosaic to a corrected LST orthomosaic. The optional spatial emissivity correction starts in the*
 250 *pink box and can be implemented in both workflows. Initial data and end products are indicated in bold, the required inputs*
 251 *are outlined in black.*

252 3.1. Data Collection

253 The initial step involves collecting the thermal images. To check if your TIR camera is compatible with
254 the workflow, execute the function `tuav_cameras()` to view a list of supported cameras. Currently the
255 package supports the following cameras: TeAx ThermalCapture (2.0), Micasense Altum(-PT), DJI Mavic
256 3T, DJI Mavic 4T, DJI Matrice 3TD, DJI Zenmuse H20N, DJI Zenmuse H20T, DJI Zenmuse H30T, DJI Matrice
257 30T (both normal and super-resolution mode). Read carefully the camera's user manual before use. It
258 is, furthermore, advisable to conduct flights under homogeneous atmospheric conditions to avoid
259 rapid transitions between sunny and cloudy conditions. To monitor atmospheric changes during the
260 flight, it is recommended to use a portable weather station capable of measuring air temperature and
261 relative humidity at high frequency, e.g. in 5-second intervals (Kelly et al., 2019; Maes, 2025). In the
262 absence of a portable weather station, data from the nearest weather station could be used. As
263 previously mentioned in Section 2.1, the background temperature (T_{bg}) can be accurately measured
264 by placing a reference panel covered with crumpled aluminium foil on the ground and obtaining the
265 corresponding brightness temperature using the TIR camera. Make sure that the aluminium foil panel
266 is large enough, so it is covered by at least 9 pixels, to avoid mixed pixels and obtain an accurate
267 reading.

268 3.2. The image-based workflow

269 3.2.1. Create ThermalUAV object

270 The image-based workflow is structured around a custom R object of class ThermalUAV. A ThermalUAV
271 object comprises lists with slots for essential variables that will be filled and used along the way,
272 facilitating a streamlined and flexible workflow. The variables are categorized into the following
273 sections: Info, Position, Sharpness, Atmosphere, Smooth and ThermalData, where the latter stores the
274 temperature data as a list of matrices (LST or brightness temperature, depending on the step and used
275 parameters). The function `tuav_create()` creates a ThermalUAV object relying on the pathname to the
276 thermal image folder, the camera name (check `tuav_cameras()`), the flight height, and optionally the
277 path to an additional metadata data frame.

278 3.2.2. Conversion of at-sensor temperature to LST

279 The function `tuav_correct()` performs the necessary corrections at the image level on a ThermalUAV
280 object, given the required atmospheric data. The atmospheric data can be provided in one of the
281 following formats: (i) a single measurement of air temperature (T_{air}) and relative humidity ($\omega\%$), (ii) T_{air}
282 and/or $\omega\%$ as vectors with lengths corresponding to the number of images in the ThermalUAV object,
283 (iii) a data frame containing T_{air} and $\omega\%$ along with datetime information covering at least the whole
284 duration of the flight, or (iv) in the absence of measured air temperature, T_{air} can also be estimated

285 using a trimmed mean from the pixel values in the thermal image. For each image, the water vapor
286 content and the transmittance is calculated using respectively Eqs. (8), (9), followed by the calculation
287 of the LST using a single emissivity value, provided by the user (Eq. (4)). In occasions where background
288 temperature (T_{bg}) was not measured, T_{bg} will be estimated following Eq. (10). The user should then
289 specify if the conditions were sky clear or overcast. The function reads the TIFF files and stores the LST
290 values as a list of matrices under ThermalData. Eventually an updated ThermalUAV object is returned
291 including the LST information. Note: if emissivity is set to 1, this function does not correct for
292 background temperature and emissivity (Eq. (4)). In that case, the returned temperature data will be
293 the brightness temperature. This is recommended if emissivity is corrected spatially afterwards (see
294 Section 3.2.4). Furthermore, *tuav_correct()* does not account for the effect of T_{air} on LST (Maes, Huete
295 and Steppe, 2017), but can be corrected using the post-processing function *tuav_smooth()* (see section
296 3.2.6).

297 3.2.3. Exporting and mosaicking

298 Once all the desired corrections have been applied, the ThermalData can be exported as geotagged
299 TIFF files using function *tuav_export()*. To efficiently store the temperature data with a two-decimal
300 precision, each image is written as centikelvin in a 16 bit TIFF file labelled
301 "original_filename_corrected.tif". These files include the necessary metadata for further processing,
302 including GNSS position and altitude, pitch, roll yaw, and more. After saving all the corrected thermal
303 images, you can align and mosaic them using commercial photogrammetry software, such as Agisoft
304 Metashape or Pix4D Mapper, to create a land surface temperature orthomosaic. Since the data is
305 stored in centikelvin, it should be divided by 100 and then subtracted by 273.15 to convert the resulting
306 temperatures to degrees Celsius. If desired an HTML-report can be created using *tuav_report()*. This
307 report provides an overview of the executed corrections with their corresponding parameters, camera
308 locations in an interactive map, and general background information about the mission.

309 3.2.4. Emissivity correction

310 When your area of interest comprises multiple land cover types and/or a heterogeneous landscape,
311 spatially explicit emissivity correction is recommended. As described in Section 3.2.2, the
312 *tuav_correct()* function uses only one emissivity value, as spatially explicit emissivity correction is not
313 accurate at the image level due to uncertainties in image positioning and viewing angles. The post-
314 processing function *tuav_emis()* does allow for emissivity correction on georeferenced LST
315 orthomosaics. To apply the emissivity correction, the pixel values are first backtransformed to at-
316 sensor temperature, given the original parameters provided in the corresponding ThermalUAV object.
317 The land surface temperature on pixel level is now calculated with a spatially explicit emissivity value
318 using one of the following methods: (i) the NDVI threshold method (as described in **Error! Reference**

319 **source not found.**), given the NDVI map and providing the necessary thresholds directly in the
 320 function; (ii) the land cover map with a two-column matrix containing the values of the land cover
 321 classes in the first column and their corresponding emissivity values in the second; or (iii) directly using
 322 an emissivity map. The LST orthomosaic and the map to be used for the correction can be provided as
 323 either a *terra::SpatRaster* object or as pathname to the map stored locally on your personal computer.

324 3.2.5. Accounting for varying weather conditions

325 Conducting thermal flight missions under stable, sunny conditions is recommended due to the
 326 challenges associated with correcting illumination changes in thermal data (Maes, 2025). Rapid
 327 changes in illumination can lead to heterogeneity and distortion in the final land surface temperature
 328 orthomosaic. While techniques such as radiometric block adjustment are employed to address this
 329 issue in multispectral UAV imagery, they remain under-investigated for thermal UAV data (Wang et al.,
 330 2024). Maes, Huete and Steppe (2017) proposed a technique to account for the effect of varying air
 331 temperature on LST using a high temporal resolution air temperature dataset:

$$T_{surf_{correct}} = T_{surf} - T_{air} + T_{air_{mean}} \quad (14)$$

332 where $T_{surf_{corrected}}$ is the corrected surface temperature (T_{surf}), T_{air} is the air temperature at the moment
 333 of image capture, and $T_{air_{mean}}$ is the mean air temperature during the flight. This correction method is
 334 incorporated in the package under the function *tuav_smooth()*, with the parameter *method* set to
 335 “*T_air*”. A limitation of this technique is its inability to capture spatially explicit changes in illumination
 336 and local wind gusts, as typically only one portable weather station is placed at a fixed location.
 337 Additionally, obtaining such a dataset is not always feasible.

338 To address these limitations, we propose a similar technique based on the temperature of the thermal
 339 images themselves. First, the trimmed mean (with a fraction of 20%) of each image in the ThermalData
 340 is calculated to avoid the influence of extreme temperatures (Eq. (15)). Second, the smoothed
 341 temperature (T_{smooth}) is calculated as the mean of a moving window with a length equal to
 342 *smoothlength* (Eq. (16)). Finally, the image is corrected by subtracting its corresponding T_{smooth} and
 343 adding the mean of T_{smooth} (Eq. (17)).

$$T_{image,mean}[i] = mean(T_{image}[i], 0.2) \quad (15)$$

$$T_{smooth}[i] = mean\left(T_{image,mean}\left[i - \frac{smoothlength}{2} : i + \frac{smoothlength}{2}\right]\right) \quad (16)$$

$$T_{image_{corrected}} = T_{image} - T_{smooth} + T_{smooth_{mean}} \quad (17)$$

344 The newly proposed method is also embedded in the function *tuav_smooth()*. To perform the
 345 correction using this method, the parameter *method* should be set to “*image*”. This correction should
 346 always be performed after calling *tuav_correct()* as it relies on the temperature data stored under

347 ThermalData in the ThermalUAV object. The performance of this correction will be discussed using a
 348 use case in Section 5.

349 3.2.6. Other functionalities

350 The R package offers additional functionalities beyond those previously described. Note, to keep a
 351 clear overview, only the basic functions are represented in Figure 2. We will briefly outline some
 352 functions in

353 Table 1, but more functions and detailed information are available in the package’s reference and
 354 vignettes. All the functions require a ThermalUAV object as input and, except *tuav_view()*, return an
 355 updated ThermalUAV object.

356 *Table 1: an overview of additional functionalities within the image-based workflow. These functions can only be applied on*
 357 *ThermalUAV objects at any time during the processing unless stated otherwise.*

	Function	Description
Position functions	<i>tuav_loc()</i>	Calculates the camera locations/image extents as <i>terra::SpatVector</i> object. Optionally the mean frontal overlap can be calculated.
	<i>tuav_view()</i>	Plots the camera locations/image extents in an interactive map. This allows for visual checks aiding in intermediate cleaning steps.
	<i>tuav_coreg()</i>	Optimizes thermal camera locations and viewing angles using co-registered high-resolution cameras with a high precision GNSS system. Can be done directly or by using the optimized camera locations after stitching the high-resolution camera in Agisoft Metashape. In the latter case <i>coreg_prep()</i> is needed to set the data in the right format. Optimized cameras are stored in an updated ThermalUAV object and are used when exporting.
Cleaning	<i>tuav_persec()</i>	Reduces the data volume by specifying the number of images to retain per second, keeping the ones with the highest sharpness. Can be useful for thermal cameras recording at a fixed high frequency rate.
	<i>tuav_reduc()</i>	Reduces the data volume either based on a minimal frontal overlap or minimal sharpness quality. Can be useful for thermal cameras recording at a fixed high frequency rate.

358 3.3. The orthomosaic-based workflow

359 The orthomosaic-based workflow corrects brightness temperature orthomosaics. This means that the
 360 raw thermal images are first stitched in a photogrammetry software. Possibly, a conversion to Kelvin
 361 might be required as some cameras provide their data as centikelvin or as DN where a linear constant
 362 should be applied. The *ortho_correct()* function relies on one value for T_{air} and $\omega\%$, as intra-flight
 363 atmospheric variability is not considered. The emissivity value can be set to a single value for the entire
 364 map, or you have the option to spatially account for it in a similar way as described in Section 3.2.4.

365 3.4. DJI Thermal IR Processing

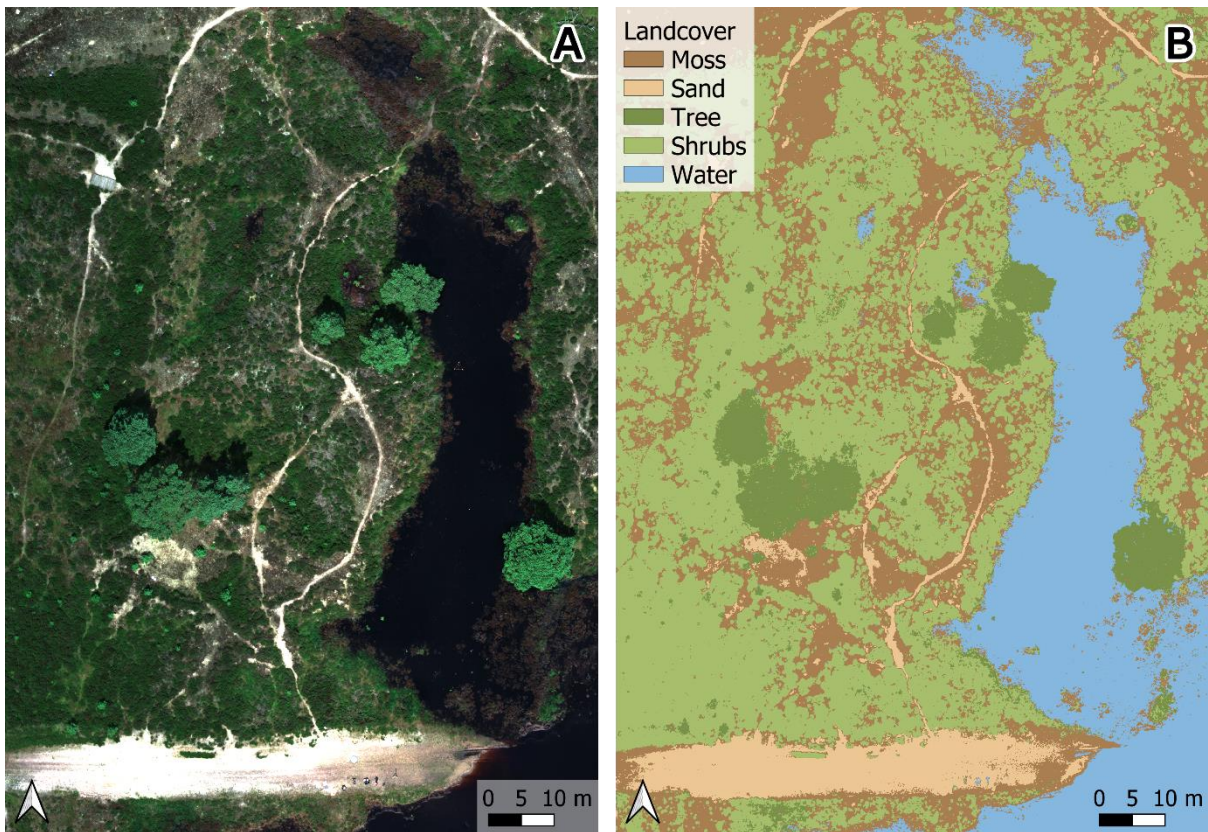
366 Thermal images captured with a DJI (Da-Jiang Innovations) camera are stored in a specific way and
 367 require preprocessing before getting to actual temperature information. Therefore, the DJI Thermal

368 IR Processing (DIRP) functionality, as used in the DJI thermal Analysis Tool, is also incorporated into the
369 R package through the function *tuav_dji()*. The function is not part of the image-based workflow as it
370 does not return a ThermalUAV object, however, it does require a ThermalUAV object as input to work
371 with the metadata. The function, furthermore, depends on object distance, relative humidity,
372 emissivity and reflected temperature to convert the data to LST. Please note should be made that the
373 underlying conversion is not made publicly available by DJI. When using the image-based workflow for
374 DJI cameras, this function is embedded in *tuav_correct()*, meaning no additional preprocessing is
375 required. In this case, the object distance is set to 1 and emissivity to 1 to achieve the at-sensor
376 temperature, on which the regular processing is performed as outlined in Section 2. There are two
377 prerequisites for using the R package for DJI cameras: (i) a version of Python must be installed on your
378 system, subsequently, a virtual environment should be initialized using the function *dji_init()*, and (ii)
379 it is only compatible with Windows and Linux systems, as the Dynamic Link Libraries provided by DJI
380 are available only for these two systems.

381 **4. Case 1: An empirical example of the Image-Based Workflow using ThermalCapture 2.0**

382 **4.1. Data collection**

383 In this section, we present an example of the image-based workflow. The study area is a heterogenous
384 patch within the Kalmthoutse Heide (**Error! Reference source not found.**A), a heathland ecosystem in
385 Belgium. The landscape consists of heather shrubs (*Calluna vulgaris*) on a sandy soil, interspersed with
386 patches of moss and bare soil, some trees (*Pinus sylvestris*), and shallow ponds (Figure 3B). A short
387 flight was conducted on July 19, 2024, at 14:00 local time under clear sky conditions. We used the DJI
388 Matrice 300 RTK equipped with (i) the Micasense Altum-PT to collect multispectral information, and
389 (ii) the TeAx ThermalCapture 2.0 with the ThermalCapture Calibrator to obtain thermal information. A
390 single grid flight mission was performed at 75 m above ground level with a side overlap of 80% and
391 flight speed of 4.5 m/s, resulting in a ground sampling distance of 3.28 cm for the multispectral data
392 and 9.66 cm for the thermal images. During the flight, free air temperature and relative humidity were
393 measured at 5-second intervals with a Kestrel 5500L environmental meter placed on a tripod of 1.5 m
394 height. Mean air temperature and relative humidity during the flight were 28.3 °C and 42.7 %,
395 respectively.



396
397
398

Figure 3. (A) RGB composite from the Micasense Altum-PT. (B) Land cover map showing the diverse landscape consisting of moss, sand, trees, shrubs and water.

399 4.2. Pre-processing

400 The multispectral imagery was processed using Agisoft Metashape Professional 2.0.0, following the
 401 recommended workflow (Agisoft Metashape, 2024). Reflectance calibration was performed using
 402 images of a 60 cm x 60 cm panel with 50 % reflectance taken at the flight altitude. As our thermal
 403 camera is co-registered with the Micasense Altum-PT, we will also demonstrate the optional co-
 404 registration workflow. Consequently, the camera references were exported as CSV file, including the
 405 rotation and estimated values with a precision of 7 decimal numbers. The thermal data, stored as TMC
 406 file, were converted to TIFF files using the ThermoViewer 3.0.10 software from TeAx. Metadata were
 407 exported as a single CSV file for all images.

408 4.3. Processing using the theRmalUAV package

409 The first step in the image-based workflow is creating the ThermalUAV object. After loading the
 410 theRmalUAV package into the environment, `tuav_create()` will create the ThermalUAV object (Section
 411 3.2.1), here named as `thermaluav`. More information can be found in the help pages of the package.

```
412 library(theRmalUAV)
413 thermaluav <- tuav_create(path = "Data/TIFs/", camera = "ThermalCapture", meta_csv =
414 "Data/TIFs/Example_meta.csv", flight_height = 75)
```


415 The ThermalCapture 2.0 is a thermal camera that records images at a rate of 8.33 Hz, resulting in a
416 dataset of 1,237 images. The function `tuav_reduc()` (

417 Table 1) is used to downsize the dataset, retaining only the sharpest images while setting a minimal
418 frontal overlap. In this case, we chose for a minimal frontal overlap of 85%, resulting in a dataset of
419 125 images. The resulting ThermalUAV object is saved as a new variable (`thermaluav_reduc`) to avoid
420 overwriting the previous ThermalUAV object.

```
421 thermaluav_reduc <- tuav_reduc(thermaluav, method = "Overlap", min_overlap = 0.85)
```

422 Corrections can now be performed using `tuav_correct()` (Section 3.2.2). As we will later perform the
423 optional, though recommended, spatially explicit emissivity correction, emissivity is initially set to 1 to
424 obtain the brightness temperature. The free air temperature and relative humidity were provided in
425 the format of a data frame obtained from the Kestrel environmental meter, allowing for image-level
426 corrections.

```
427 thermaluav_correct <- tuav_correct(thermaluav_reduc, flight_height = 75, T_air = Kestrel, rel_hum = Kestrel,  
428                                  T_bg = 274.2, emiss = 1)
```

429 To correct for the effect of air temperature on the surface temperature, we can use the function
430 `tuav_smooth()` (

431 Table 1).

```
432 thermaluav_smooth <- tuav_smooth(thermaluav_correct, method = "T_air")
```

433 In our camera setup, the ThermalCapture 2.0 is fixed to our Micasense Altum-PT, allowing us to co-
434 register the thermal data and benefit from the RTK accuracy of the Altum-PT camera. First, the data
435 must be converted into the correct format using `coreg_prep()`. This function relies on camera
436 references of the Altum-PT, which were exported from Agisoft Metashape, as mentioned in Section 0.
437 Subsequently, the co-registration is performed using `tuav_coreg()`. Here, the rig offset values are
438 provided in millimetres and are measured to the green band of the Altum-PT (band 2, the band to
439 which other bands are offset). More information can be found in the vignettes and the help pages of
440 the package.

```
441 sfm_cameras <- coreg_prep(img_path = "Data/Micasense/000/", SfM_option = "Agisoft Metashape",  
442                          opt_camera_path = "Data/Micasense/ReferenceCameras_example.txt",  
443                          camera_name = "Altum-PT_MSP", label = "_2", timezone = "UTC")  
444 thermaluav_coreg <- tuav_coreg(thermaluav_smooth, opt_cameras = sfm_cameras, rig_offset = c(-46,-103,-20,  
445                                             0, 0, 0))
```

446 Finally, we can export the data stored in the final ThermalUAV object. In this case, the ThermalData
447 contains brightness temperatures as we used an emissivity of 1, and the camera locations were
448 optimized during the co-registration. The information can be exported as TIFF files using `tuav_export()`.

```
449 tuav_export(thermaluav_coreg)
```

450 The TIFF files were processed in Agisoft Metashape using default parameters (Align > Build Point Cloud
 451 > Build DEM > Build Orthomosaic). The obtained orthomosaic was converted to degrees Celsius and
 452 exported as a GeoTIFF. To achieve land surface temperatures, we need to account for emissivity. The
 453 spatially explicit emissivity correction in this example is performed using the land cover option in the
 454 function *tuav_emis()*. First, a matrix is made linking the land cover labels to their corresponding
 455 emissivity (Table 2; (Rubio et al., 1997).

456 *Table 2. Land cover classes with their corresponding emissivity values.*

Label	Land cover	Emissivity
1	Dry mosses	0.962
2	Sand	0.914
3	Tree	0.983
4	Shrubs	0.984
5	Water	0.991

457 The function also requires the original temperature GeoTIFF - here the brightness temperature built in
 458 Agisoft Metashape -, a map to base our corrections on - here the land cover map -, and the last
 459 ThermalUAV object related to this project.

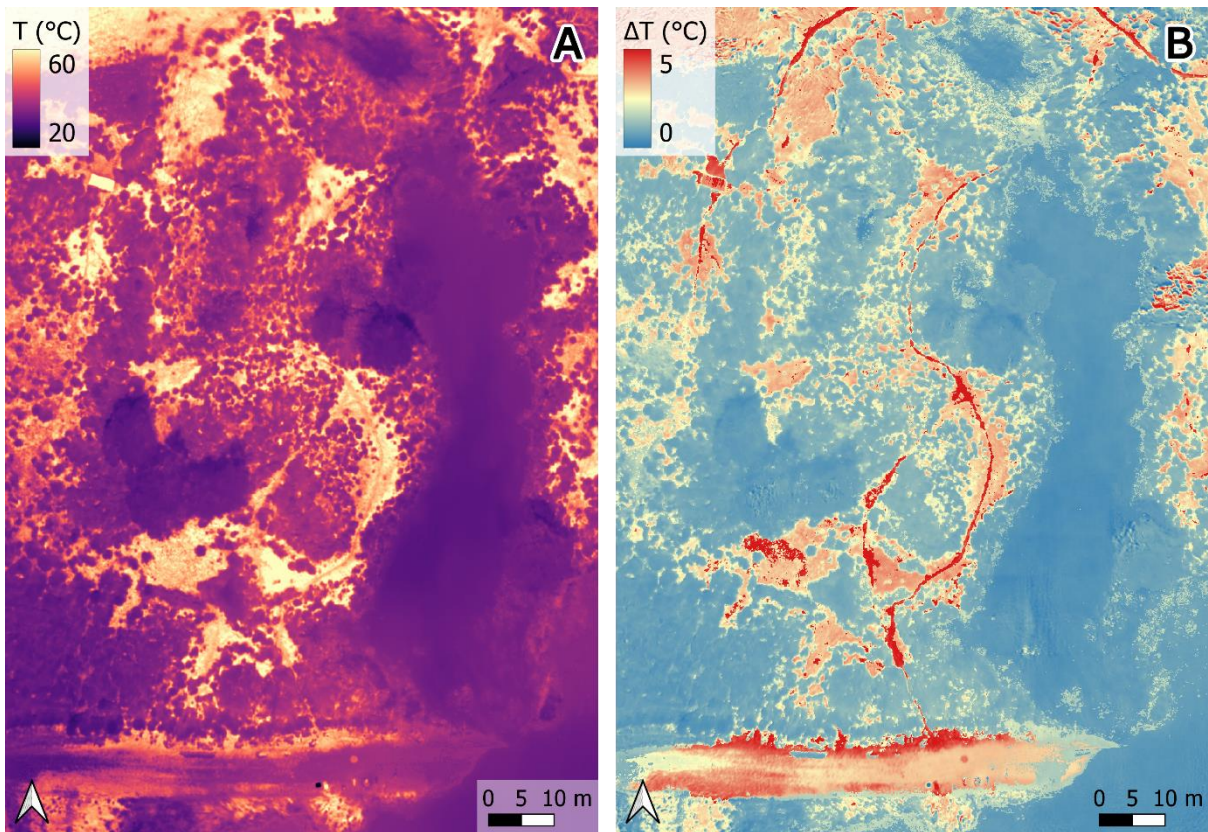
```

460 matrix <- matrix(c(1,2,3,4,5,0.962,0.914,0.983,0.984,0.991), ncol = 2)
461 thermaluav_emis <- tuav_emis(thermal_orig = "Data/Example_Tbright.tif",
462                             thermal_uav = thermaluav_coreg,
463                             temp = "C",
464                             corrmatrix = "Data/Example_LC.tif",
465                             method = "LC",
466                             write_Ts = TRUE,
467                             filename_Ts = "Example_Tsurf.tif",
468                             LC_emiss_matrix = matrix)
  
```

469 4.4. Results

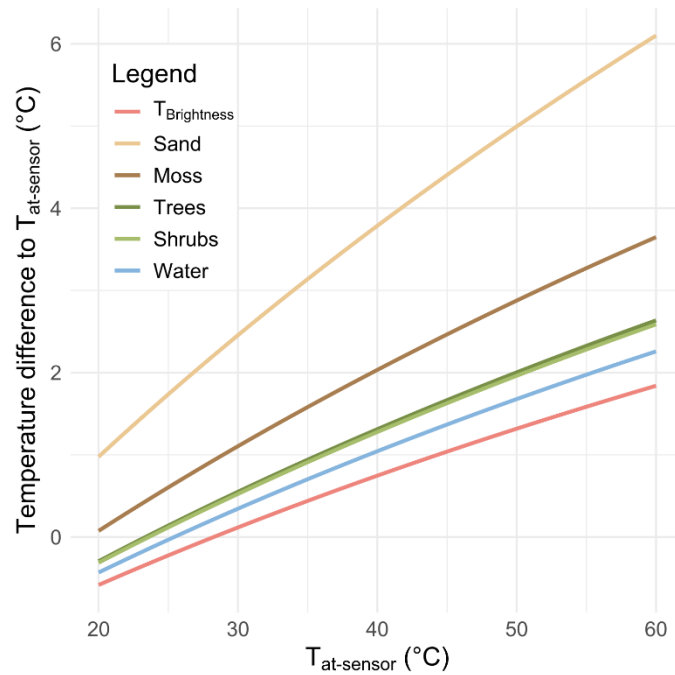
470 The final LST map illustrates **Error! Reference source not found.** the wide range of temperatures in this
 471 heterogeneous landscape on a hot, sunny day (Figure 4A). The bare sandy areas reach temperatures
 472 up to 50 °C, while the dark, dry mosses exhibit extreme surface temperatures up to 60°C due to the
 473 absorption of shortwave solar radiation and a lack of evapotranspiration. The shallow, still pond had a
 474 surface temperature of approximately 31°C.

475 The at-sensor temperature substantially underestimates the LST, with temperature differences
 476 reaching up to 5°C in certain instances (Figure 4B). The largest discrepancies are observed in areas with
 477 extreme temperatures and land covers with low emissivity values (e.g., bare sand, Figure 3B). The
 478 waterbody and trees, which generally have lower temperatures and emissivity values nearing 1, show
 479 smaller discrepancies (around 0.5°C).



480
 481 *Figure 4. (A) Final LST map of the area representing the temperatures in degree Celsius. (B) Temperature difference (ΔT)*
 482 *between the LST and the at-sensor temperature.*

483 To provide more insight into the effect of the corrections for this example, the differences between a
 484 range of at-sensor temperatures and the final LST per land cover class (and thus, emissivity), as well as
 485 the brightness temperature, are plotted in **Error! Reference source not found.**. These differences were
 486 calculated using Eq. (6) with the mean atmospheric conditions during the flight: a transmittance of
 487 0.9368, air temperature of 28.26 °C and a background temperature of 274.2 K. The emissivity values
 488 for each class are shown in Table 2, and to obtain the brightness temperature, the emissivity was set
 489 to 1. Note that the influence of the atmospheric correction is minimal when the at-sensor temperature
 490 approximates the free air temperature but becomes significant at very high temperatures (up to 2 °C
 491 in this example). When accounting for emissivity and background temperature, the discrepancies
 492 become more prominent, especially at extreme temperatures and where the surface substantially
 493 deviates from the black body behaviour. This trend aligns with Figure 4B, where the largest
 494 discrepancies occur on the bare soil (low emissivity) and at the patches of dry moss (extreme
 495 temperatures).

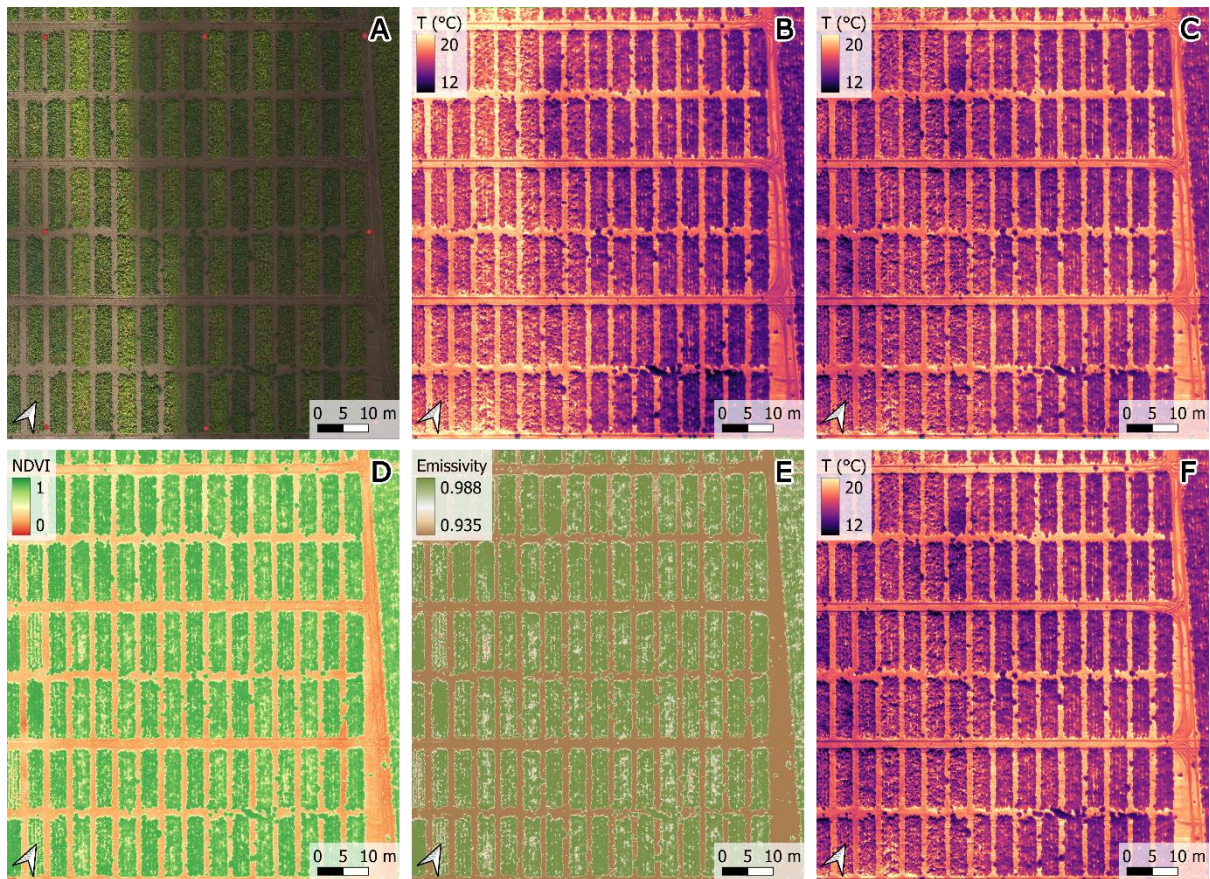


496 *Figure 5: Temperature differences to the at-sensor temperature in sunny conditions for Case 1. With the brightness*
 497 *temperature ($\epsilon = 1$) in red becoming higher compared to at-sensor temperature when the at-sensor temperature exceeds the*
 498 *free air temperature. The differences to the final LST are given per land cover class as they each have a different emissivity*
 499 *($\epsilon_{\text{sand}} = 0.914$, $\epsilon_{\text{moss}} = 0.962$, $\epsilon_{\text{tree}} = 0.983$, $\epsilon_{\text{shrub}} = 0.984$, $\epsilon_{\text{water}} = 0.991$). The differences are calculated using Eq. (6) with the*
 500 *mean atmospheric values during the flight: a transmittance of 0.9368, air temperature of 28.26 °C and a background*
 501 *temperature of 274.2 K.*

502 **5. Case 2: Accounting for variable weather conditions using the DJI Mavic 3T**

503 **5.1. Data Collection**

504 In this second use case, we demonstrate the effect of the smoothing function *tuav_smooth()* on a flight
 505 conducted under variable weather conditions. The flight took place on September 13, 2024, at 12:25
 506 local time over a potato field in Bottelare, Belgium. Initially, the flight conditions were sunny, but a
 507 cloud quickly covered the area, drastically altering the illumination (Figure 6A). The average air
 508 temperature was 16.1 °C, and the relative humidity was measured at 98 %. Thermal images were
 509 acquired using a DJI Mavic 3T at a flight altitude of 30 m. To generate the corresponding NDVI map
 510 (Figure 6D), we used the Micasense RedEdge Dual mounted on a DJI Matrice 350 RTK, earlier the same
 511 day under stable weather conditions. Eight ground control points (GCPs) were spread out across the
 512 field to align the thermal data with the NDVI map.



513

514 *Figure 6. Potato field in Bottelare, Belgium. (A) RGB orthomosaic derived from the RGB camera on the DJI Mavic 3T,*
 515 *simultaneously captured with the thermal data, showing the fast change in illumination going from left to right. The red dots*
 516 *represent the locations of the ground control points. (B) Brightness temperature in °C before using the smoothing function,*
 517 *clearly showing the same pattern as the RGB data, influenced by the change in weather conditions. (C) Brightness temperature*
 518 *in °C after using the smoothing function, accounting for this change, resulting in a more homogenous output. (D) the*
 519 *corresponding NDVI map created from the Micasense RedEdge Dual, flown earlier that day under stable, sunny conditions.*
 520 *(E) Emissivity map of the field, the NDVI threshold method gives more nuances and a continuum of emissivity values between*
 521 *the thresholds. (F) Final LST in °C, where the warm bare soil, clearly defines the colder vegetation plots and the artefact of the*
 522 *varying weather conditions is accounted for.*

523 5.2. The effect of `tuav_smooth()`

524 In this example, we used a DJI thermal camera. To work with the DJI cameras, the function `dji_init()`
 525 must first be called to set up the necessary configurations and access the Thermal SDK functionality
 526 embedded in the package (see Section 3.4). Similar to the empirical example in Section 4, we began
 527 by creating a ThermalUAV object using `tuav_create()`, specifying the path to the image folder and the
 528 camera name. Subsequently, the correction function was applied. In this case, we used a single value
 529 for air temperature (T_{air}) and relative humidity (rel_hum). Background temperature was not
 530 measured and thus was estimated using Eq. (10). As the majority of the flight was under overcast
 531 conditions, `SKC` was set to `FALSE`. Emissivity was set to 1, as spatial emissivity correction would be
 532 performed later, providing us with the brightness temperature. The data was then exported.

```
533 library(theRmalUAV)
534 dji_init()
535 path <- "H:/Thermal_Project/Data/M3T/"
```

```

536 thermaluav <- tuav_create(path = path, camera = "DJI_M3T")
537 thermaluav_correct <- tuav_correct(thermaluav, T_air = 16.1, rel_hum = 98, T_bg = NA, emiss = 1, SKC = FALSE)
538 tuav_export(thermaluav_correct)

```

539 To account for the effect of illumination changes during the flight, we applied the function
540 *tuav_smooth()* using the method “*image*” (Section 3.2.5). The “*smooth_length*” parameter was set to
541 the number of images in one flight line, excluding the turns. The smoothed images were also exported.

```

542 thermaluav_smooth <- tuav_smooth(thermaluav_correct, method = "image", smooth_length = 16)
543 tuav_export(thermaluav_smooth)

```

544 The exported images, containing the smoothed and non-smoothed brightness temperatures, were
545 aligned and mosaicked in Agisoft Metashape Professional 2.0.0. The orthomosaic of the non-smoothed
546 brightness, clearly shows the large change in illumination, leading to a substantial impact on the
547 temperature data (Figure 6B). Conversely, the smoothed dataset produced a much more homogenous
548 orthomosaic, effectively accounting for the change in illumination (Figure 6C).

549 5.3. Spatial emissivity correction using NDVI

550 With the smoothed brightness temperature orthomosaic and the corresponding NDVI map, we
551 performed spatial emissivity correction to obtain the LST. Similar to Section 4.3, we used the
552 *tuav_emis()* function, but now with the method *NDVI* (Section 3.2.4). This method relies on four
553 thresholds (Section 2.2). The NDVI values for soil (*NDVI_{soil}*) and vegetation (*NDVI_{veg}*) were estimated
554 using our NDVI map, set at 0.3 and 0.88, respectively. Emissivity values for soil (*emiss_{soil}*) and vegetation
555 (*emiss_{veg}*) were set at 0.935 and 0.988, respectively (Heinemann et al., 2020).

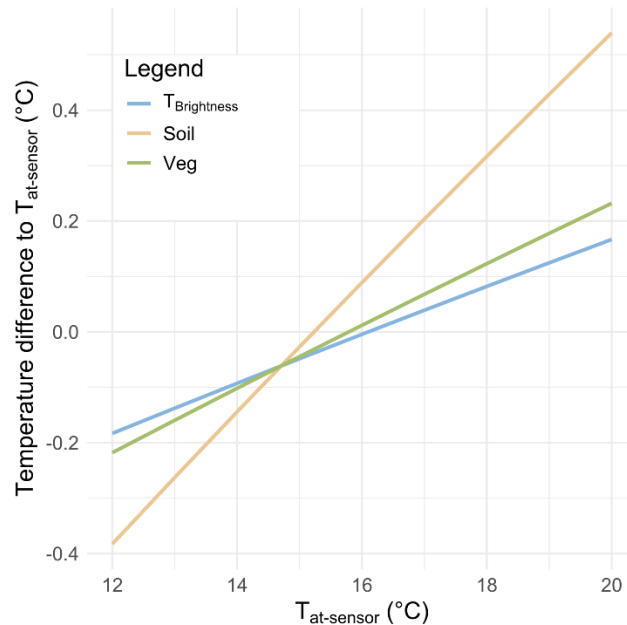
```

556 NDVI <- terra::rast("H:/Thermal_Project/Data/M3T/250913_NDVI.tif")
557 T_bright_smooth <- terra::rast("H:/Thermal_Project/Data/M3T/TBright_smooth_orthomosaic.tif")
558 Thermaluav_emis <- tuav_emis(thermal_orig = T_bright_smooth,
559                             thermal_uav = thermaluav_smooth,
560                             temp = "C",
561                             corrmmap = NDVI,
562                             method = "NDVI",
563                             write_Ts = TRUE,
564                             filename_Ts = "Potato_LST_smooth.tif",
565                             write_emiss = TRUE,
566                             NDVI_veg = 0.88,
567                             NDVI_soil = 0.3,
568                             emiss_veg = 0.988,
569                             emiss_soil = 0.935,
570                             filename_emiss = "Potato_emis.tif")

```

571 Using the NDVI threshold method provides more nuances in emissivity values (Figure 6E). As both
572 brightness temperature (*T_{bright}*) and background temperature (*T_{bg}*) are close to the free air
573 temperature, the effect of emissivity is smaller compared to Case 1 (Section 4). The final LST reaches
574 slightly higher values compared to *T_{bright}* where the at-sensor temperature (*T_{at-sensor}*) is higher compared
575 to *T_{bg}* (287.80 K; 14.65 °C). This is especially the case where emissivity is lower (e.g., the bare soil paths

576 between the vegetation; Figure 6F). On locations where $T_{at-sensor}$ is lower than T_{bg} , the final LST is lower
 577 compared to T_{bright} . To provide more insight, the above-mentioned relations are plotted in Figure 7.



578
 579 *Figure 7. Temperature differences to the at-sensor temperature ($T_{at-sensor}$) in overcast conditions for Case 2. With the brightness*
 580 *temperature ($\epsilon = 1$) in blue becoming higher compared to $T_{at-sensor}$ when $T_{at-sensor}$ exceeds the free air temperature. The*
 581 *differences to the final LST are given for soil ($\epsilon_{soil} = 0.935$) and vegetation ($\epsilon_{veg} = 0.988$). The differences are calculated using*
 582 *Eq. (6) with the mean atmospheric values during the flight: a transmittance of 0.9581, air temperature of 16.1 °C and a*
 583 *background temperature (T_{bg}) of 287.80 K. When $T_{at-sensor}$ exceeds T_{bg} the LST becomes higher compared to the brightness*
 584 *temperature due to emissivity values lower than 1. The difference becomes higher with a lower emissivity value.*

585 6. Conclusion

586 The theRmalUAV R-package integrates the latest correction methods discussed in the literature into a
 587 flexible and user-friendly open-source tool. This package aims to facilitate the necessary corrections
 588 required to obtain LST from thermal UAV cameras. The thermal remote sensing background section
 589 clarifies the physics underlying the package, highlighting the importance of these corrections and
 590 addressing the knowledge gap in the use and processing of thermal UAV imagery.

591 The package offers two distinct workflows: an image-based workflow and an orthomosaic-based
 592 workflow. The orthomosaic workflow applies the necessary corrections at the orthomosaic level using
 593 a single function, while the image-based workflow provides additional functionalities. These include
 594 accounting for intra-flight variations in atmospheric conditions and thus atmospheric corrections (e.g.,
 595 transmittance), as well as the effect of air temperature on surface temperature. Additionally, a novel
 596 method for addressing rapid changes in illumination, using temperature data from the images
 597 themselves, results in more homogeneous orthomosaics with fewer artifacts.

598 Other functionalities of the package encompass data cleaning, co-registration, and reporting.
 599 Furthermore, the importance of the spatial emissivity correction is emphasized, with both the NDVI
 600 method and a land cover method incorporated into both workflows. The functionalities are

601 demonstrated through two use cases, with further details available in the package’s help function and
602 vignettes. The theRmalUAV R-package performs complete image processing while retaining the
603 necessary metadata for alignment and mosaicking in photogrammetry software.

604 **Declaration of Competing Interest**

605 None.

606 **Funding**

607 This study was funded by Internal Funds of KU Leuven (MICROMICS project; C14/22/067).

608 **Declaration of generative AI and AI-assisted technologies in the writing process.**

609 During the preparation of this work the lead author used Microsoft Copilot in order to improve the
610 readability and language of the manuscript. After using this tool, the author reviewed and edited the
611 content as needed and takes full responsibility for the content of the published article.

612 **Acknowledgements**

613 The author would like to thank Wouter H. Maes for the valuable insights in thermal UAV remote
614 sensing and the first idea of the script, Koenraad Van Meerbeek for the constructive feedback
615 regarding the storyline and Sam Ottoy for support regarding UAV field campaigns.

616 **References**

617 Agisoft Metashape, 2024. MicaSense Altum processing workflow (including Reflectance Calibration)
618 in Agisoft Metashape Professional [WWW Document]. URL
619 [https://agisoft.freshdesk.com/support/solutions/articles/31000148381-micasense-altum-](https://agisoft.freshdesk.com/support/solutions/articles/31000148381-micasense-altum-processing-workflow-including-reflectance-calibration-in-agisoft-metashape-professi)
620 [processing-workflow-including-reflectance-calibration-in-agisoft-metashape-professi](https://agisoft.freshdesk.com/support/solutions/articles/31000148381-micasense-altum-processing-workflow-including-reflectance-calibration-in-agisoft-metashape-professi)

621 Aicardi, I., Chiabrando, F., Lingua, A.M., Noardo, F., Piras, M., Vigna, B., 2017. A methodology for
622 acquisition and processing of thermal data acquired by UAVs: a test about subfluvial springs’
623 investigations. *Geomatics, Natural Hazards and Risk* 8, 5–17.
624 <https://doi.org/10.1080/19475705.2016.1225229>

625 Allison, R.S., Johnston, J.M., Craig, G., Jennings, S., 2016. Airborne optical and thermal remote
626 sensing for wildfire detection and monitoring. *Sensors (Switzerland)* 16.
627 <https://doi.org/10.3390/s16081310>

628 Beaver, J.T., Baldwin, R.W., Messinger, M., Newbolt, C.H., Ditchkoff, S.S., Silman, M.R., 2020.
629 Evaluating the Use of Drones Equipped with Thermal Sensors as an Effective Method for
630 Estimating Wildlife. *Wildl Soc Bull* 44, 434–443. <https://doi.org/10.1002/wsb.1090>

631 Budzier, H., Gerlach, G., 2015. Calibration of uncooled thermal infrared cameras. *Journal of Sensors*
632 *and Sensor Systems* 4, 187–197. <https://doi.org/10.5194/jsss-4-187-2015>

633 Carlson, T.N., Ripley, D.A., 1997. On the relation between NDVI, fractional vegetation cover, and leaf
634 area index. *Remote Sens Environ* 62, 241–252. [https://doi.org/10.1016/S0034-4257\(97\)00104-](https://doi.org/10.1016/S0034-4257(97)00104-1)
635 [1](https://doi.org/10.1016/S0034-4257(97)00104-1)

636 Cheng, K.H., Jiao, J.J., Luo, X., Yu, S., 2022. Effective coastal *Escherichia coli* monitoring by unmanned
637 aerial vehicles (UAV) thermal infrared images. *Water Res* 222, 118900.
638 <https://doi.org/10.1016/j.watres.2022.118900>

639 Cuenca, J., Sobrino, J., 2004. Experimental measurements for studying angular and spectral variation
640 of thermal infrared emissivity. *Appl Opt* 43, 4598–4602. <https://doi.org/10.1364/AO.43.004598>

- 641 Dai, G., Wang, C., Tang, Q., He, L., Chen, H., Sunil, C.K., Dewi, C., 2025. Aerial infrared thermal
642 imaging transmission line defect detection methods incorporating explicit visual center
643 structures. *Measurement (Lond)* 245, 116605.
644 <https://doi.org/10.1016/j.measurement.2024.116605>
- 645 Frolec, J., Králík, T., Musilová, V., Hanzelka, P., Srnka, A., Jelínek, J., 2019. A database of metallic
646 materials emissivities and absorptivities for cryogenics. *Cryogenics (Guildf)* 97, 85–99.
647 <https://doi.org/10.1016/j.cryogenics.2018.12.003>
- 648 Heinemann, S., Siegmann, B., Thonfeld, F., Muro, J., Jedmowski, C., Kemna, A., Kraska, T., Muller, O.,
649 Schultz, J., Udelhoven, T., Wilke, N., Rascher, U., 2020. Land surface temperature retrieval for
650 agricultural areas using a novel UAV platform equipped with a thermal infrared and
651 multispectral sensor. *Remote Sens (Basel)* 12. <https://doi.org/10.3390/rs12071075>
- 652 Henn, K.A., Peduzzi, A., 2024. Surface Heat Monitoring with High-Resolution UAV Thermal Imaging:
653 Assessing Accuracy and Applications in Urban Environments. *Remote Sens (Basel)* 16.
654 <https://doi.org/10.3390/rs16050930>
- 655 Hoffmann, H., Nieto, H., Jensen, R., Guzinski, R., Zarco-Tejada, P., Friborg, T., 2016. Estimating
656 evaporation with thermal UAV data and two-source energy balance models. *Hydrol Earth Syst*
657 *Sci* 20, 697–713. <https://doi.org/10.5194/hess-20-697-2016>
- 658 Hoffrén, R., García, M.B., 2023. Thermal unmanned aerial vehicles for the identification of
659 microclimatic refugia in topographically complex areas. *Remote Sens Environ* 286.
660 <https://doi.org/10.1016/j.rse.2022.113427>
- 661 Jones, H., Vaughan, R., 2010. Remote sensing of vegetation principles techniques and applications.
662 Oxford university press.
- 663 Jones, H.G., Archer, N., Rotenberg, E., Casa, R., 2003. Radiation measurement for plant
664 ecophysiology. *J Exp Bot* 54, 879–889. <https://doi.org/10.1093/jxb/erg116>
- 665 Kelly, J., Kljun, N., Olsson, P.-O., Mihai, L., Liljeblad, B., Weslien, P., Klemedtsson, L., Eklundh, L., 2019.
666 Challenges and Best Practices for Deriving Temperature Data from an Uncalibrated UAV
667 Thermal Infrared Camera. *Remote Sens (Basel)* 11. <https://doi.org/10.3390/rs11050567>
- 668 Kerr, Y.H., Lagouarde, J.P., Nerry, F., Ottlé, C., 2004. Land surface temperature retrieval techniques
669 and applications, in: Quattrochi, D.A., Luvall, J.C. (Eds.), *Thermal Remote Sensing in Land*
670 *Surface Processing*. CRC Press, p. 464. [https://doi.org/https://doi.org/10.1201/9780203502174](https://doi.org/10.1201/9780203502174)
- 671 Li, Z.L., Becker, F., 1993. Feasibility of land surface temperature and emissivity determination from
672 AVHRR data. *Remote Sens Environ* 43, 67–85. [https://doi.org/10.1016/0034-4257\(93\)90065-6](https://doi.org/10.1016/0034-4257(93)90065-6)
- 673 Li, Z.L., Wu, H., Wang, N., Qiu, S., Sobrino, J.A., Wan, Z., Tang, B.H., Yan, G., 2013. Land surface
674 emissivity retrieval from satellite data. *Int J Remote Sens* 34, 3084–3127.
675 <https://doi.org/10.1080/01431161.2012.716540>
- 676 Liao, K.C., Lu, J.H., 2021. Using uav to detect solar module fault conditions of a solar power farm with
677 ir and visual image analysis. *Applied Sciences (Switzerland)* 11, 1–21.
678 <https://doi.org/10.3390/app11041835>
- 679 Lillesand, T.M., Kiefer, R.W., Chipman, J.W., 2015. Remote sensing and image interpretation, 7th ed.
680 ed. Wiley, Hoboken, NJ.

- 681 Maes, W.H., 2025. Practical Guidelines for Performing UAV Mapping Flights with Snapshot Sensors.
682 Remote Sens (Basel) 17. <https://doi.org/10.3390/rs17040606>
- 683 Maes, W.H., Huete, A.R., Steppe, K., 2017. Optimizing the processing of UAV-based thermal imagery.
684 Remote Sens (Basel) 9. <https://doi.org/10.3390/rs9050476>
- 685 Maes, W.H., Steppe, K., 2012. Estimating evapotranspiration and drought stress with ground-based
686 thermal remote sensing in agriculture: a review. J Exp Bot 63, 4671–4712.
687 <https://doi.org/10.1093/jxb/ers165>
- 688 Manfreda, S., McCabe, M.F., Miller, P.E., Lucas, R., Madrigal, V.P., Mallinis, G., Dor, E. Ben, Helman, D.,
689 Estes, L., Ciraolo, G., Müllerová, J., Tauro, F., de Lima, M.I., de Lima, J.L.M.P., Maltese, A.,
690 Frances, F., Caylor, K., Kohv, M., Perks, M., Ruiz-Pérez, G., Su, Z., Vico, G., Toth, B., 2018. On the
691 use of unmanned aerial systems for environmental monitoring. Remote Sens (Basel) 10.
692 <https://doi.org/10.3390/rs10040641>
- 693 Messina, G., Modica, G., 2020. Applications of UAV thermal imagery in precision agriculture: State of
694 the art and future research outlook. Remote Sens (Basel). <https://doi.org/10.3390/RS12091491>
- 695 Minkina, W., Klecha, D., 2015. Modeling of Atmospheric Transmission Coefficient in Infrared for
696 Thermovision Measurements 903–907. <https://doi.org/10.5162/irs2015/1.4>
- 697 Mirka, B., Stow, D.A., Paulus, G., Loerch, A.C., Coulter, L.L., An, L., Lewison, R.L., Pflüger, L.S., 2022.
698 Evaluation of thermal infrared imaging from uninhabited aerial vehicles for arboreal wildlife
699 surveillance. Environ Monit Assess 194, 1–15. <https://doi.org/10.1007/s10661-022-10152-2>
- 700 Muro, J., Strauch, A., Heinemann, S., Steinbach, S., Thonfeld, F., Waske, B., Diekkrüger, B., 2018. Land
701 surface temperature trends as indicator of land use changes in wetlands. International Journal
702 of Applied Earth Observation and Geoinformation 70, 62–71.
703 <https://doi.org/10.1016/j.jag.2018.02.002>
- 704 Posch, C., Matolin, D., Wohlgenannt, R., Maier, T., Litzenberger, M., 2009. A microbolometer
705 asynchronous dynamic vision sensor for LWIR. IEEE Sens J 9, 654–664.
706 <https://doi.org/10.1109/JSEN.2009.2020658>
- 707 Rakha, T., Liberty, A., Gorodetsky, A., Kakillioglu, B., Velipasalar, S., 2018. Heat Mapping Drones: An
708 Autonomous Computer-Vision-Based Procedure for Building Envelope Inspection Using
709 Unmanned Aerial Systems (UAS). Technology Architecture and Design 2, 30–44.
710 <https://doi.org/10.1080/24751448.2018.1420963>
- 711 Rubio, E., Caselles, V., Badenas, C., 1997. Emissivity measurements of several soils and vegetation
712 types in the 8–14 μm wave band: Analysis of two field methods. Remote Sens Environ 59, 490–
713 521. [https://doi.org/10.1016/S0034-4257\(96\)00123-X](https://doi.org/10.1016/S0034-4257(96)00123-X)
- 714 Rudol, P., Doherty, P., 2008. Human body detection and geolocalization for UAV search and rescue
715 missions using color and thermal imagery. IEEE Aerospace Conference Proceedings.
716 <https://doi.org/10.1109/AERO.2008.4526559>
- 717 Salisbury, John W., D’Aria, D.M., 1992. Emissivity of terrestrial materials in the 8–14 μm atmospheric
718 window. Remote Sens Environ 42, 83–106. [https://doi.org/10.1016/0034-4257\(92\)90092-X](https://doi.org/10.1016/0034-4257(92)90092-X)
- 719 Santesteban, L.G., Di Gennaro, S.F., Herrero-Langreo, A., Miranda, C., Royo, J.B., Matese, A., 2017.
720 High-resolution UAV-based thermal imaging to estimate the instantaneous and seasonal

721 variability of plant water status within a vineyard. *Agric Water Manag* 183, 49–59.
722 <https://doi.org/10.1016/j.agwat.2016.08.026>

723 Sedlar, J., Hock, R., 2009. Testing longwave radiation parameterizations under clear and overcast
724 skies at Storglaciären, Sweden. *Cryosphere* 3, 75–84. <https://doi.org/10.5194/tc-3-75-2009>

725 Sobrino, J.A., El Kharraz, J., Li, Z.L., 2003. Surface temperature and water vapour retrieval from
726 MODIS data. *Int J Remote Sens* 24, 5161–5182.
727 <https://doi.org/10.1080/0143116031000102502>

728 Sobrino, J.A., Jiménez-Muñoz, J.C., Sòria, G., Romaguera, M., Guanter, L., Moreno, J., Plaza, A.,
729 Martínez, P., 2008. Land surface emissivity retrieval from different VNIR and TIR sensors. *IEEE*
730 *Transactions on Geoscience and Remote Sensing* 46, 316–327.
731 <https://doi.org/10.1109/TGRS.2007.904834>

732 Sobrino, J.A., Raissouni, N., 2000. Toward remote sensing methods for land cover dynamic
733 monitoring: Application to Morocco. *Int J Remote Sens* 21, 353–366.
734 <https://doi.org/10.1080/014311600210876>

735 Stutsel, B., Johansen, K., Malbêteau, Y.M., McCabe, M.F., 2021. Detecting Plant Stress Using Thermal
736 and Optical Imagery From an Unoccupied Aerial Vehicle. *Front Plant Sci* 12.
737 <https://doi.org/10.3389/fpls.2021.734944>

738 Tang, B.H., Shao, K., Li, Z.L., Wu, H., Tang, R., 2015. An improved NDVI-based threshold method for
739 estimating land surface emissivity using MODIS satellite data. *Int J Remote Sens* 36, 4864–4878.
740 <https://doi.org/10.1080/01431161.2015.1040132>

741 Tran, Q.H., Han, D., Kang, C., Haldar, A., Huh, J., 2017. Effects of ambient temperature and relative
742 humidity on subsurface defect detection in concrete structures by active thermal imaging.
743 *Sensors (Switzerland)* 17, 1–18. <https://doi.org/10.3390/s17081718>

744 Valor, E., Caselles, V., 1996. Mapping land surface emissivity from NDVI: Application to European,
745 African, and South American areas. *Remote Sens Environ* 57, 167–184.
746 [https://doi.org/10.1016/0034-4257\(96\)00039-9](https://doi.org/10.1016/0034-4257(96)00039-9)

747 Van de Griend, A.A., Owe, M., 1993. On the relationship between thermal emissivity and the
748 normalized difference vegetation index for natural surfaces. *Int J Remote Sens* 14, 1119–1131.
749 <https://doi.org/10.1080/01431169308904400>

750 Vlaminck, M., Heidbuchel, R., Philips, W., Luong, H., 2022. Region-Based CNN for Anomaly Detection
751 in PV Power Plants Using Aerial Imagery. *Sensors* 22, 1–18. <https://doi.org/10.3390/s22031244>

752 Wang, Y., Yang, Z., Khan, H.A., Kootstra, G., 2024. Improving Radiometric Block Adjustment for UAV
753 Multispectral Imagery under Variable Illumination Conditions. *Remote Sens (Basel)* 16, 1–27.
754 <https://doi.org/10.3390/rs16163019>

755 Wood, R.A., Han, C.J., Kruse, P.W., 1992. Integrated uncooled infrared detector imaging arrays, in:
756 *Technical Digest IEEE Solid-State Sensor and Actuator Workshop*. pp. 132–135.
757 <https://doi.org/10.1109/SOLSEN.1992.228308>

758 Wu, Y., Shan, Y., Lai, Y., Zhou, S., 2022. Method of calculating land surface temperatures based on the
759 low-altitude UAV thermal infrared remote sensing data and the near-ground meteorological
760 data. *Sustain Cities Soc* 78, 103615. <https://doi.org/10.1016/j.scs.2021.103615>

